Corrosion Properties of Powder Bed Fusion Additively Manufactured 17-4 PH Stainless Steel

Rebecca F. Schaller, Jason M. Taylor*, Jeffrey Rodelas*, and Eric J. Schindelholz***

Center for Materials Science and Engineering, Sandia National Laboratories.

ARTICLE INFO

Article history:

Keywords:

A. Porosity
B. Additive Manufacturing (AM)
C. Micro-electrochemical Cell
D. Crevice Corrosion
E. Powder Metallurgy

*Sandia National Laboratories, PO Box 5800, MS 0889, Albuquerque, NM, 87185-0889.

**Corresponding author: 505-845-8695.
Email: ejschi@sandia.gov.

ABSTRACT

The corrosion susceptibility of a laser powder bed fusion (LPBF) additively manufactured alloy, UNS S17400 (17-4 PH), was explored compared to conventional wrought material. Microstructural characteristics were characterized and related to corrosion behavior in quiescent, aqueous 0.6 M NaCl solutions. Electrochemical measurements demonstrated that the LPBF 17-4 PH alloy exhibited a reduced passivity range and active corrosion compared to its conventional wrought counterpart. A micro-electrochemical cell was employed to further understand the effects of the local scale and attributed the reduced corrosion resistance of the LPBF material to pores with diameters ≥ 50 μm.

SAND2016-12748J

INTRODUCTION

Metal additive manufacturing (AM) has recently become a desirable process for complex parts across a broad range of applications.[1] Laser powder bed fusion (LPBF) is an AM process for metals whereby a laser is used to selectively melt a pattern in successive layers of powder material as a means of building a three dimensional structure. The locally high cooling rates produced during the process with highly non-equilibrium solidification conditions result in microstructures that can vary significantly from traditional wrought materials.[2, 3] The LPBF processes can create material that often contains substantial solute segregation with formation of terminal solidification phases. It can also contain unprocessed particles from the starting powder resulting in pores.[2, 3] As a consequence of these varied microstructures, AM alloys may exhibit properties vastly different to their conventional wrought or cast counterparts.[4, 5] For example, Yadollahi reported that fatigue cycles for a range of stress amplitudes for 17-4 PH AM in the H1050 condition were nearly an order of magnitude less than wrought material. This was ascribed to the large number of defects in the AM material, including pores, un-melted regions and un-melted powder particles.[6] Mower et. al. found AM 17-4 PH displayed a considerably diminished yield strength compared to wrought material (610 to 737 MPa versus 898 MPa) and attributed this to incomplete fusion across build planes in the AM process.[7] While some adjustments have been made in manufacturing to enhance mechanical traits, such as incorporation of carbide particles into the powder mixture for strengthening, very little attention has been directed at understanding or controlling the corrosion properties of these materials.[8, 9]

In this study we explore the relative impact of microstructural characteristics unique to AM processing on the corrosion properties of LPBF 17-4 PH stainless steel (UNS S17400). Specifically, and for the first time, we investigate the corrosion behavior of a 17-4 PH LPBF material under full immersion saline conditions and provide comparison to conventional wrought 17-4 PH stainless steel. Studies on 300 series AM stainless steels suggest porosity of these materials can considerably increase corrosion susceptibility, but lack direct evidence of the influence of pores on corrosion properties.[3, 10] Here we utilized both bulk and local electrochemical measurements to relate microstructural features to corrosion behavior, including the role of pores on passivity. The results presented provide important feedback for enhancement of AM processing techniques to optimize corrosion properties.

Background

Studies to date of LPBF manufactured stainless steels have uncovered substantially higher corrosion susceptibility compared to wrought counterparts. It has been suggested that elemental segregation, residual oxides from initial powders, and porosity, similar to characteristics seen in more conventional powder metallurgy (PM) materials, may be at fault.[3, 11, 12] AM materials are expected to exhibit reduced corrosion properties similar to conventional PM materials due to the comparable microstructures formed from processing.[12]

In PM stainless steels, elemental segregation from non-equilibrium processing conditions reduce the corrosion resistance of the materials compared to conventional wrought or cast equivalents. Chromium depletion of stainless steels is of particular concern as it results in regions with reduced or unstable oxides that can lead to locally sensitive areas prone to corrosion attack.[13] Samal demonstrated that hydrogen sintered 316 stainless steel (UNS S31600) processed with a range of cooling rates and carbon content (0.01 to 0.11 % C), resulted in a range of sensitized material. The authors applied a critical cooling temperature curve for wrought 316 L to avoid sensitization, showing a consistent correlation between sensitization and corrosion rates for the 316L PM samples.[14]

Initial studies of AM processed stainless steel exhibit trends similar to PM materials regarding corrosion resistance and elemental segregation of passivating elements. Trelewicz et al. found that micro-segregation in AM materials depreciates their corrosion properties. Segregation of Mo in 316L due to LPBF processing increased the passive current

density of the AM material by almost an order of magnitude in 0.1 M HCl solution.[11]

Elevated oxygen content in PM alloys originating from starting powders is known to cause a considerable decrease in corrosion resistance, a highly probable scenario for AM materials as well. Oxide formation originates from relatively large amounts of pre-existing oxides on the high surface area starting powder. These oxides are not always reduced in the furnaces, and can lead to a reduction in the pitting potential of PM steels.[15-17] Klar et al reported a strong dependence of 316L corrosion initiation time (with visible surface staining or rust on the surface) in 5 wt% NaCl electrolyte on oxygen content, whereby initiation time was near 10^4 h for 250 ppm oxygen and decreased to less than 0.5 h for 1750 ppm.[16, 17]

The inherently porous nature of PM stainless steels has been demonstrated to play a governing role in their reduced passivity.[12, 18, 19] Pore geometry and interconnectivity are two critical factors that can govern occluded cell-type corrosion susceptibility. Pores breaching the material surface with favorable attributes in this regard can serve as crevice zones wherein IR drop and maintenance of acidic, hydrolytic conditions can enable depassivation within the pores. One study on 304L and 316L exposed to ferric chloride solutions, resulted in primary corrosion attack occurring within pores.[19] Similar results on 304L and 316L were seen in sulfuric and phosphoric acid. The authors attributed this attack to local acidification within the pore, resulting in depassivation of the material and the formation of an active region within the pore supported by cathodic activity outside the pore.[18]

Investigators have demonstrated general trends between porosity and corrosion resistance, but this is complicated by the aforementioned factors and environment. Jones reported that corrosion resistance of three austenitic stainless steels with varying weight percent Ni improved with decreased porosity for a sintered density range of 6.25 to 7.25 g/cm^3, in acid media, 40% HNO_3.[20] However in saline solutions, the relationship between material density and corrosion susceptibility was complicated further by pore geometry on 316L. At high porosity and large pore size, ≥ 20 µm, little to no crevice corrosion was promoted. At intermediate porosity, high corrosion occurred as the pores are narrow(≤ 20 µm) promoting hydrolysis leading to crevice corrosion, and at high density, few pores existed to promote crevice corrosion.[21, 22] A similar relationship between corrosion rate and pore size for 316L was shown for atmospheric salt fog exposures, where corrosion rate was inversely related to the pore diameter.[23]

Examinations have shown that localized corrosion attack on AM materials can also be initiated by defects, such as elongated grains, heterogeneities,[11] and porosity.[10] Porosity and surface roughness was shown to play a large role on corrosion properties of AlMgSi direct metal laser sintered alloys, where even in the polished condition, remaining pores exhibited enhanced corrosion attack in SEM micrographs.[10] While these studies provide initial insight into the corrosion behavior of AM materials there is a lack in the literature for results relating direct, local scale exploration of either the chemical or morphological microstructural characteristics of AM materials on the corrosion properties of the material.

In this study we explore the properties of wrought and LPBF 17-4 PH in the H900 temper condition via full immersion and local micro-electrochemical measurements in 0.6 M NaCl solution to establish a baseline. Correlation is drawn between the measured corrosion behavior and microstructural features characterized via optical and electron microscopy techniques before and after electrochemical interrogation. The results provide direct evidence of the primary governance of pores on the decreased corrosion resistance of the LPBF material. We discuss the mechanisms behind the effect of porosity on corrosion behavior, future investigations necessary for enhanced understanding, and possible solutions/ suggestions for AM processing to enhance the corrosion resistance of these materials.

EXPERIMENTAL PROCEDURES

Materials

Additively manufactured samples of 17-4 PH stainless steel were compared to conventional wrought samples. The AM materials, acquired commercially, were printed via a laser powder bed fusion process, in which feedstock powder was sintered in a pre-programmed pattern in successive layers by a laser. All LPBF 17-4PH specimens were heat treated to industrial material standards (AMS 5604) by solution heat treating at 1050°C for 60 minutes in argon atmosphere and subsequently cooled to room temperature. Both AM and wrought specimens were then age hardened to the H900 condition by heating to 482°C for 60 minutes in air.

All sample surfaces tested or examined were ground to 1200 grit silicon carbide paper, polished to 1 µm diamond paste, cleaned with 18.2 MΩ deionized water, IPA, and dried with nitrogen. The top surface was selected for study here as it was the surface available in a testable sample size, Figure 1. Samples of the wrought material were prepared in the same manner. Polished LPBF samples for bulk electrochemical experiments were tested both prior to and post-sonication in DI water, and no significant difference was observed. However, materials for micro-scale experiments were sonicated to avoid influence of possible trapped polishing particles.

Material Characterization

Material characterization of the LPBF and wrought 17-4 PH was carried out to determine both composition and microstructure. Compositional analysis of the as-received materials was determined via inductively coupled plasma atomic emission spectroscopy (ICP-AES) and ICP-mass spectrometry (MS) for Cr, Ni, Mn, Cu, Si, Mo, P, Cb, and Ta and LECO furnace analysis for C,S,O, and N. Fe was determined by the difference in the above mentioned measurements. Microstructural analysis comprised standard optical metallurgical examination along with scanning electron microscopy (SEM), energy dispersive spectroscopy (EDS), and wavelength dispersive X-ray spectroscopy (WDS). Light optical microscopy was performed on polished sections etched using Viella's reagent which is comprised of a solution of 100 mL ethanol, 1 g picric acid, and 5 mL concentrated hydrochloric acid. As-polished samples were utilized for other analyses. SEM/EDS was carried out at 20 keV at high vacuum mode and at a working distance of 9 to 12 mm using a Zeiss field emission source SEM. EDS signals were normalized to the maximum peak (Fe K-α). Electron probe microanalysis (EPMA) via WDS was performed using a JEOL JXA-8530F HyperProbe Electron Probe Microanalyzer. High-resolution beam scan maps were acquired using an accelerating voltage of 15 keV with a beam current of 20 nA using a point-to-point spacing of 0.1 µm. A ZAF correction procedure was utilized to produce quantitative elemental maps of the LPBF 17-4PH microstructure.

Pore number density and size distribution in the build direction plane and perpendicular to the build direction plane, shown in Figure 1, were estimated via image analysis of secondary electron micrographs and optical images. ImageJ software was applied for this analysis using a threshold procedure.[24] A minimum of three images were analyzed for

each direction, providing pore distribution and size information on the build direction plane and perpendicular plane.

Electrochemical Methods

Electrochemical experiments were carried out using either a standard three electrode flat cell to characterize bulk behavior or a micro-electrochemical three electrode cell to target behavior of specific surface features. The electrolyte used for all experiments was ambiently aerated pH 6, 0.6 M NaCl solution prepared with 18.2 MΩ deionized water. All electrochemical experiments were evaluated at room temperature (23 °C).

Both open circuit potential (E_{OCP}) and potentiodynamic polarizations were carried out in the flat cell. A saturated calomel electrode (SCE) was used as the reference electrode and PtNb mesh as the counter electrode. Prior to potentiodynamic measurements, samples were held at open circuit potential for 1 or 24 hours to allow materials to come to steady state. Anodic and cathodic potentiodynamic scans were conducted at a scan rate of 0.1667 mV/s after the open circuit holds. A minimum of 5 replicate scans for each material and condition were conducted.

A micro-electrochemical cell method following procedures outlined elsewhere was used to locally target surfaces with different pore size populations.[25-31] The micro-electrochemical cell used consisted of a silicone tipped glass capillary, with an inner diameter of 380 µm connected to a cell body containing a Pt wire as a counter electrode and chloridized silver wire as a reference. The chloridized silver wires were made following the procedures developed by Hassel et al., and allowed to stabilize in 0.6 M NaCl for 12 h.[32] Measurements were made by touching down the cell filled with 0.6 M NaCl solution to targeted areas on the LPBF and wrought samples to create a seal. Open circuit potential measurements were then taken for 1 and 24 h along with subsequent potentiodynamic measurements at a scan rate of 1 mV/s. A faster scan rate was selected for the micro-electrochemical cell than that used in full immersion experiments to avoid H_2 bubbles during initial cathodic polarization that could block the capillary and to minimize changes in solution chemistry in the capillary. No crevice corrosion was observed after electrochemical testing. The microelectrochemical cell will aid in establishing the influence of pore size populations, large vs. small, on the corrosion behavior of the LPBF material.

Full Immersion Exposures

Polished AM samples were immersed in ambiently aerated 0.6 M NaCl solution up to 7 days. After exposure, samples were rinsed with deionized water, sonicated for a minimum of five minutes to remove excess salt solution, and dried with nitrogen prior to imaging in the SEM.

RESULTS

Sample Characterization

Compositions of the LPBF vs. the wrought 17-4 PH studied here are presented in Table 1. Figure 6 is a micrograph showing the typical appearance of the etched microstructure of wrought and AM 17-4PH samples. This material can be characterized as a martensitic matrix with a relatively fine (~10-20 µm) prior austenite grain size with interspersed islands of delta-ferrite. No evidence of solidification substructure can be observed in these micrographs (Figure 6).

Pore distribution and microstructural morphology of the LPBF material are exemplified in SEM micrographs in Figures 3 and 4 and in the EPMA images in Figure 5. Larger pores (d > 50 µm) exhibit very irregular shapes and can contain remaining unsolidified particles, whereas smaller pores (d <10 µm) are typically more hemispherical in shape (noted in Figure 4.a). These smaller, spherical pores have been observed in other AM materials and can be attributed to gas porosity rather than unmelted regions within the LPBF sample.[1, 33] Figure 4 shows a higher magnification image of a typical pore in which unsolidified powder particles from the printing process can be seen (a). An EDS scan was taken of the entire area, displaying even Cr distribution across the entire surface (b, within the pore, line of sight to the EDS detector limits some detection of Cr). Three spectra are shown for comparison, from the undissolved particle, the inner surface of the pore, and the general polished surface of the LPBF material, showing no considerable gross difference in elemental composition among these three regions. High-resolution EPMA maps (Figure 5) of the LPBF specimens after heat treatment show a lack of discernable microsegregation in the martensitic matrix (again within the pore, line of sight to the WDS detector limits some detection of Cr). Local enrichment of Nb and Si/O corresponding to Nb-carbonitrides and Si-rich oxides is observed.

Measurements of the maximum pore diameter on the top surface and cross-section of the 17-4 PH AM material, Figure 1, reveal similar populations in both directions (Figure 2). The average diameter was found to be 14 µm for the top surface ranging from 3 to 273 µm and 13 µm for the cross-sectional surface ranging from 3 to 295 µm (the smallest detectable features were in the range of 2 to 4 µm at the magnification taken in the SEM). The percent area coverage was 3 ± 0.7% for the top surface and 2.4 ± 0.2% for the cross-sectional surface. For all electrochemical testing, the top, parallel to the print plane, surface was examined as it was the readily available surface available in the dimensions necessary for testing. However, as the distribution and cross-sectional geometry of the pores seen on the cross-sectional surface did not differ greatly from the top surface, similar electrochemical results would be expected.

Full Immersion Electrochemical Analysis

Representative open circuit potentials vs time for 24 h exposures are plotted in Figure 7. The E_{OCP} of the wrought material rises gradually with time. However, for the LPBF material, the E_{OCP} changes erratically over the exposure time and appears to stabilize after about 19 h of exposure. In addition, the E_{OCP} of the LPBF sample is lower than that of the wrought material.

A comparison of the average E_{OCP} from the 1 and 24 h scans were calculated and then compared to typical values from the literature for wrought 17-4 PH in Table 2. Values for the wrought sample tested at 1 h are comparable (within 30 mV) to those found in literature for 17-4 PH stainless steels tested for 15 min to 40 h.

Representative anodic polarizations after one hour at E_{OCP} displayed different behavior between wrought and LPBF 17-4 PH. The wrought material exhibited spontaneous passivity, whereas the LPBF material exhibited higher anodic currents with no region of apparent passivity. Current densities were approximately 2 orders of magnitude greater over the same voltage range (Figure 8). However, for the anodic scans taken post 24 h E_{OCP}, both the LPBF sample and wrought sample exhibited passive regions. Again, the current densities were higher by about 2 orders of magnitude. Cathodic scans for both wrought and

LPBF samples post 1 h E_{OCP} displayed similar behaviors, with a lowered E_{OCP} for the LPBF material (Figure 9), indicating similar behavior in cathodic kinetics for the surface of both samples.

A comparison of the open circuit corrosion current densities estimated for each material (i_{corr}) for the LPBF vs wrought 17-4 PH samples are given in Table 2. These were calculated using the Tafel slope extrapolation, however are meant as indicators rather than true corrosion current densities as 17-4 PH exhibits passive behavior with pitting corrosion rather than general corrosion. It is interesting to note that the LPBF samples demonstrate a higher corrosion current density, nearly an order of magnitude, for the anodic scans taken post 1 and 24 h holds at the E_{OCPs}.

Micro-electrochemical Measurements

The results of the micro-electrochemical cell analysis for the 1 h E_{OCP} are plotted in Figure 10.a, and display no considerable differences between the large pore ($d \geq 50$ µm) and small pore ($d \leq 10$ µm) surfaces. Small pores are included in both scan measurements, as they are distributed fairly evenly across the LPBF surface and were unavoidable in the current measurement technique. However, as can be seen in Figure 10.b, the anodic scan taken above the large pore surface showed increased current densities with no apparent passive region and a lower E_{OCP} than the small pore surface. The scan above the small pore demonstrated a passive region, more similar to that of the wrought material. A micro-electrochemical scan of a wrought sample is also plotted in Figure 10.b. A comparison of i_{corr} values for the LPBF 17-4 PH large pores, small pore surfaces, and wrought material are given in Table 3. These are again meant only as an indication of local passive current densities. In this case the current densities are much closer and no significant difference is seen between the i_{corr} of the large pores and the small pore surfaces. As a comparison, E_{OCP} holds were taken for 24 h followed by anodic scans and are plotted in Figure 11. As can be seen, the E_{OCP} for the larger pore is lower and less stable than that of the smaller pores. However, both anodic scans display a large passive region more similar to that of the wrought material (Figure 11.b).

Exposures

Post-exposure, for samples immersed in 0.6 M NaCl solution for 1 week, SEM imaging was applied and images for a LPBF sample are shown in Figure 12. Corrosion product can be seen forming near and around pores or possible pits. While these are smaller scale pores, $d \approx 10 - 20$ µm, they still exhibit irregular shapes with crevice-like regions due to lack of fusion during processing.

Discussion

The LPBF 17-4 PH material examined in this study displayed inferior corrosion resistance with increased passive current density and a decrease in the passive region compared to wrought 17-4 PH materials in the same environment. Previous studies of PM materials bearing similar microstructural and morphological features have attributed this to elemental segregation, retained oxides, and/ or porosity as discussed earlier. In this study, the presence of pores was found to be the primary contributing factor to corrosion susceptibility. The following discussion rationalizes this finding.

Material composition analysis given in Table 1 shows the LPBF samples are within the accepted typical requirements for 17-4 PH. Conventional wrought 17-4 PH is a precipitation hardened stainless steel, with 15-17.5 Cr wt %. At this elemental composition, this alloy is close to the lower limiting composition of what is considered a stainless steel; 11 wt% Cr.[34] The amount of Cr is limited in this alloy to allow for a fully transformed martensitic structure at room temperature. Simple empirically-derived relationships originally proposed by Eichelmann and Hull were used to relate alloy composition and the start temperature of the martensite transformation.[35] For the alloys examined here, all LPBF samples possessed an estimated M_s temperature between 265 and 285°C. For comparison, the estimated M_s temperature for wrought 17-4PH sheet was 248°C. While such temperatures are empirical estimates, such calculated transformation temperatures are indicative of the precondition of austenite instability at room temperature for 17-4PH. However, as the Cr composition of 17-4 PH is close to passivity limits, any changes to the microstructure, either in elemental segregation, oxide formation, or morphology may affect the corrosion susceptibility of the material as they could easily disrupt the passivating oxide layer.

The melting and rapid solidification of 17-4PH during laser powder bed fusion processes results in microstructural features distinct from thermomechanically-processed material such as sheet. Characteristic features from the solidification process include relatively large solidification grains that grow preferentially along an axis aligned toward the moving heat source. Moreover, solidification grains will also contain substructure which is formed by operative solute redistribution during non-equilibrium solidification.[36] For precipitation-strengthened martensitic stainless steels including LPBF 17-4PH, heat treatment of the as-fabricated material is required to produce desired mechanical and corrosion behavior. Figure 6 shows light optical micrographs of etched AM 17-4PH microstructures for the corrosion tests examined in this work. The complete lack of solidification features in the heat treated LPBF 17-4PH samples indicates the 1050°C solutionization heat treatment resulted in recrystallization. The heat treatment also led to homogenization of solute microsegregation and the subsequent microstructure was lacking in obvious microscale features expected to lead to gross reduction in passivity. Both EDS and WDS elemental maps exhibited elemental uniformity across the samples, Figures 5 and 6. It has already been seen that Cr depletion around Cr carbides that precipitate in these conventional materials during hardening can result in a more active pitting potential by 20 to 60 mV in 3.5 wt% NaCl solution.[34] Furthermore, as the C and N compositions were 0.017 and 0.036 wt% respectively, no chromium carbides or chromium nitrides, associated with Cr depletion and sensitization, were observed through WDS.

While PH martensitic stainless steels typically have improved corrosion properties compared to martensitic stainless steels[37], the precipitation hardening process can slightly reduce the corrosion resistance of these steels due to the formation of precipitates.[34] Elevated amounts of niobium carbonitrides and silicon oxides relative to conventional wrought were present in the LPBF samples. These were small and evenly distributed throughout the surface, and not localized at the pores (Figure 5). Niobium carbonitrides have been found beneficial to the corrosion resistance of stainless steels as they suppress the formation of chromium carbides.[38] With respect to silicon oxides, it has been previously established that increased amounts of Si can actually enhance corrosion resistance in stainless steel alloys.[39, 40] However, Castle et al. have also found that pitting can occur at corrosively inert oxides with some dissolution of the oxide.[41] While silicon oxide particles in the LPBF material could contribute to

enhanced corrosion, they are not believed to be a dominant microstructural factor as evidenced by the micro-eletrochemical cell experiments.

The primary difference found between the LPBF samples and conventional wrought material is the high porosity seen in the materials in Figures 2 and 3. Two distinct morphologies were observed, large, irregular shaped pores (d > 50 μm) due to lack of fusion defects (Figure 4.a) and smaller, spherical pores (d < 10 μm) formed by gas entrapment and coalescence during processing (Figure 5.a). The influence of these structures on the corrosion behavior of the LPBF material is evident in the electrochemical results.

Electrochemical measurements of the open circuit potential provide insight into the origin of decreased passivity of the LPBF samples, exhibiting lower and more unstable E_{OCPs} than the wrought material (Tables 2 & 3, and Figure 7). This behavior is consistent with previous work on porous powder metallurgy samples relative to their wrought counterparts.[42-44] Instabilities in the E_{OCP} of the LPBF samples could be due to solution ingress into the pores or active corrosion/pitting (Figure 7 and 11).[44, 45] The overall decreased potential on the LPBF sample could be a sign of thinning or localized attack of the passive film whereas the rise in the E_{OCP} of the wrought material is indicative of an increase in the passive film thickness on the material over time.[45] Another possibility for this change in potential is related to the polarizability of the stainless steel, in that the surface potential could be easily affected by the localized corrosion events occurring across the surface.

Anodic polarization scans revealed reduced corrosion resistance for the LPBF samples as compared to the wrought material, but also a dependence on pre-exposure time. It is interesting to note that the LPBF samples pre-exposed to a 24 h E_{OCP} displayed a passive region in the anodic scan (Figure 8-b), while those pre-exposed for only one hour at E_{OCP} did not (Figure 8-a). One possible explanation for this phenomenon could be that the conditions within the pores change significantly such that they do not meet critical crevice conditions either through growth of the pore that changes the critical geometry or through a change in solution chemistry.[46] Thus these sites may deactivate as regions for enhanced anodic dissolution and the material exhibits a passive region more similar to that of the wrought material. This is evident through the anodic scans of large and small pores after a 24 h E_{OCP} hold shown in Figure 11. The E_{OCP} holds still display a lower, more unstable E_{OCP} over the 24 h period for the larger pore sample (Figure 11.a). However, the anodic scans post-24 h E_{OCP} hold result in a larger passive region for the large pore sample, indicating passivation of the pore surface with time (Figure 11.b).

The additional LPBF surface area imparted by porosity likely does not account for the five to ten times higher open circuit corrosion currents estimated for the LPBF samples relative to wrought (Table 2). Assuming the LPBF pores are hemispherical and using the measured pore size and distribution in Figure 2, we can estimate that their presence would only increase the surface area by a factor of 1.06. This is insufficient to account for the disparities in the current density measured. This is further verified through cathodic polarization scans (Figure 9) displaying the same current density for both samples indicating measurements were made from the same surface area. It must be recognized however that these larger diameter pores are not hemispherical, nor do they have a smooth round surface (Figures 3 & 4) Results from micro-electrochemical cell experiments provide further insight into these enhanced corrosion rates.

Micro-electrochemical cell experiments established that pore features directly affect the passivity of the AM stainless steel. In Figure 10, anodic polarizations over areas with large pores (d > 50 μm) exhibit active corrosion behavior with increased current density over the same voltage range. This is in contrast to passive behavior comparable to that of the wrought material witnessed in areas with few small pores (d < 10 μm). The average breakdown potentials of the large pores are more than 300 mV below that of the wrought material, 311 ± 27 mV_{SHE} for the large pores compared to 743 ± 5 mV_{SHE} for the wrought material. Breakdown potentials at small pores are more comparable to the wrought material at 577 ± 70 mV_{SHE}. This behavior changed after a 24 h E_{OCP} hold. Anodic scans on large pores exhibited a passive region with still a lower E_{OCP} suggesting passivation of the pore surface occurred during the E_{OCP} hold. The enhanced corrosion behavior of the LPBF 17-4PH material is primarily due to the presence of large pores at the sample surface. This effect may be related to pore geometry where crevice corrosion can initiate in large pores as they tend to have more narrow crevice-like geometries due to unmelted powder particles vs. smaller hemispherical pores formed by gas coalescence. Further indication of enhanced corrosion at pores was seen post-exposure in full immersion, where corrosion appeared at or near pores, Figure 12.

As pores can act as occluded areas that deplete in oxygen and become acidified during initial stages of corrosion, they can be even more conducive for corrosion attack.[47] Mathiesen et al. observed a geometrical dependence for corrosion on PM materials in that pores of a smaller diameter (d) had a higher corrosion severity.[48] An empirical relationship was previously developed for atmospheric salt fog exposures of PM 316L, in which corrosion severity, was found inversely proportional to the pore diameter.[23] This suggests, as pore diameter decreases, corrosion severity increases. However, this does not account for any limit to the enhancement of the severity as d tends to zero for the pores, which would be expected as in that case the material should resemble a conventional wrought alloy. This relation also lacks a parameter that would provide information about the aspect ratio of the pore. Pore geometry relationships can be compared to traditional crevice corrosion geometry relationships; Oldfield and Sutton found a strong dependence of crevice pH on crevice depth, thus deeper crevices could establish more severe environments for corrosion attack.[49] The interplay of pore diameter and crevice solution can affect the depth of the active/passive region, where the depth of attack increases to a limit for a wider crevice gap and a specific crevice depth.[50] Others have established a scaling law between the geometry of a crevice and the corrosion susceptibility, where the relationship between maximum crevice attack, x_{crit}, and the crevice gap, G, is either x_{crit}^2/G or x_{crit}/G, depending on the passivity of the crevice walls and whether it was IR controlled crevice corrosion.[51-53] Therefore, both pore diameter and depth can affect corrosion attack.

In the current work, larger pores were seen to exhibit a more reduced passive region and enhanced corrosion currents compared to the smaller pores in the micro-electrochemical experiments. This may have to do more with pore geometry rather than size. Larger pores, formed from lack of fusion, appeared more varied in shape with regions that could be considered tight crevices as seen in Figure 4.a. Smaller pores were generally formed due to gas coalescence, and were hemispherical in shape, lacking the tight crevices that drive the occluded cell corrosion (Figure 5.a). More detailed investigation of the relationship between pore geometry and its effect on corrosion rate would aid in understanding the influence of pore size, morphology, and

density on corrosion susceptibility in LPBF materials. Possible application of crevice modeling to pore geometries in AM materials could aid in understanding the severity of pores in terms of corrosion resistance.

As this study has found porosity to be the primary contributing factor for enhanced corrosion of AM materials, possible solutions for reducing corrosion susceptibility should include processing to reduce surface porosity. Solutions for decreasing the corrosion susceptibility of PM materials with respect to surface roughness have been previously explored. Grinding, turning, or shot blasting surfaces can seal surface pores and improve their corrosion resistance.[54] Thermal and/or chemical passivation processes can alter the oxide layers and improve corrosion resistance.[54, 55] These or similar techniques could be applied to AM materials to alleviate the negative effects of porosity on corrosion.

Conclusions

Through electrochemical measurements and immersion exposures, we found that LPBF 17-4 PH exhibited reduced corrosion resistance compared to conventional wrought 17-4 PH material in 0.6 M NaCl. Porosity was identified as the primary cause of the decreased corrosion resistance.

- Microstructural evaluation of the LPBF 17-4 PH material revealed porosity to be an obvious differentiating feature of consequence to passivity compared to wrought 17-4 PH samples. Cr segregation was not believed to greatly affect the corrosion properties as heat treatments were carried out for homogenization of solutes. Oxides in the LPBF material may play a role, but were not the dominant factor in 17-4 PH.

- The LPBF versus conventional wrought material exhibited decreased corrosion resistance through electrochemical testing. Enhanced corrosion rates on the LPBF samples over the wrought samples were indicated by the calculated i_{corr} values for the full immersion electrochemical experiments.

- Micro-electrochemical cell experiments established that the presence of pores on the sample surface directly effects the corrosion type, exhibiting active corrosion above the large pores ($d \geq 50$ μm) rather than the passive behavior displayed above regions with smaller pores ($d \leq 10$ μm) and on wrought material.

- Further evidence of enhanced corrosion at pores was confirmed by post-exposure analysis of full immersion exposures, where corrosion appeared to initiate at or near pores.

- Further understanding of the influence of porosity, such as pore size and aspect ratio, on the corrosion properties of LPBF stainless steels could help to optimize processing parameters or post-processing procedures to enhance corrosion resistance. For the material under study here, a decrease in the larger range of porosity resultant from lack of powder fusion, either through processing or post-processing treatments would be expected to dramatically enhance corrosion resistance.

Acknowledgements

The authors gratefully acknowledge Bonnie McKenzie for SEM and EDS measurements and analysis, Alice Kilgo for metallographic sample preparation, and Dick Grant for EPMA and WDS measurements. Sandia National Laboratories is a multi-program laboratory managed and operated by Sandia Corporation, a wholly owned subsidiary of Lockheed Martin Corporation, for the U.S. Department of Energy's National Nuclear Security Administration under contract DE-AC04-94AL85000.

References

1. W.E. Frazier, *J Mater Eng Perform* 23, 6 (2014): p. 1917-1928.
2. L. Thijs, F. Verhaeghe, T. Craeghs, J. Van Humbeeck, J.P. Kruth, *Acta Mater* 58, 9 (2010): p. 3303-3312.
3. M.R. Raza, F. Ahmad, M.A. Omar, R.M. German, *J Mater Process Tech* 212, 1 (2012): p. 164-170.
4. M. Mani, B. Lane, A. Donmez, S. Feng, S. Moylan, R. Fesperman, "Measurement Science Needs for Real-Time Control of Additive Manufacturing Powder Bed Fusion Processes," 2015.
5. A. Wegner, G. Witt, *Physcs Proc* 39, (2012): p. 480-490.
6. A. Yadollahi, N. Shamsaei, S. Thompson, A. Elwany, L. Bian, *International Journal of Fatigue*, (2016):
7. T.M. Mower, M.J. Long, *Mat Sci Eng a-Struct* 651, (2016): p. 198-213.
8. A. Hedge, A. Patil, V. Tambrallimath, *International Journal of Engineering Research and Technology* 3, 12 (2014): p. 14-17.
9. A.P.I. Popoola, *Int J Electrochem Sc* 9, 3 (2014): p. 1273-1285.
10. M. Cabrini, S. Lorenzi, T. Pastore, S. Pellegrini, D. Manfredi, P. Fino, S. Biamino, C. Badini, *J Mater Process Tech* 231, (2016): p. 326-335.
11. J.R. Trelewicz, G.P. Halada, O.K. Donaldson, G. Manogharan, *Jom-Us* 68, 3 (2016): p. 850-859.
12. I. Costa, S.O. Rogero, M. Saiki, R.A. Marques, J.R. Rogero, *Mater Sci Forum* 591-593, (2008): p. 18-23.
13. R.L. Sands, G.F. Bidmead, D.A. Oliver, *Modern Developments in Powder Metallurgy*, (1966): p. 73-83.
14. P.K. Samal, J.B. Terrell, in *On the Intergranular Corrosion of P/M 316l Stainless Steel*, ed. eds. V. Arnhold, C.L. Chu, W.F. Jandeska , H.I. Sanderow, ed., vol. 7 Compilers, 2002), p. 7-101.
15. R. Baboian, in *Corrosion Tests and Standards Manual*, ed. M.A. Streicher, ed.ASTM, 1995), p. 197-217.
16. E.K. D.H. Ro, *Modern Developments in Powder Metallurgy* 13, (1980): p. 247-287.
17. E. Klar, M. Svilar, C. Lall, H. Tews, *Advances in Powder Metallurgy & Particulate Materials - 1992, Vol 5*, (1992): p. 411-426.
18. E. Otero, A. Pardo, M.V. Utrilla, E. Saenz, J.F. Alvarez, *Corrosion Science* 40, 8 (1997): p. 1421-1434.
19. E. Otero, A. Pardo, M.V. Utrilla, E. Saenz, F.J. Perez, *Materials Characterization* 35, (1995): p. 145-151.
20. F.M.F. Jones, *Progress in Powder Metallurgy* 30, (1970): p. 25-50.
21. P.K.S. E. Klar, in *Corrosion Tests and Standards Manual*, ed. R. Baboian, ed., vol. MNL20-2ND ASTM, 1995), p. 551-557.
22. E. Klar, P.K. Samal, *Adv Pm Part*, (1994): p. 239-251.
23. P.K. Samal, E. Klar, *Powder Metallurgy of Stainless Steels*, ASM International, 2007).

24. W. Rasband, "Imagej Software," National Institute of Health, 2010,
25. T. Suter, H. Bohni, *Electrochim Acta* 47, 1-2 (2001): p. 191-199.
26. T. Suter, H. Bohni, *Electrochim Acta* 43, 19-20 (1998): p. 2843-2849.
27. N. Birbilis, R.G. Buchheit, *J Electrochem Soc* 152, 4 (2005): p. B140-B151.
28. N. Birbilis, M.A. Easton, A.D. Sudholz, S.M. Zhu, M.A. Gibson, *Corrosion Science* 51, 3 (2009): p. 683-689.
29. M.M. Lohrengel, *Corros Eng Sci Techn* 39, 1 (2004): p. 53-58.
30. R.G. Buchheit, R.K. Boger, M.C. Carroll, R.M. Leard, C. Paglia, J.L. Searles, *Jom-J Min Met Mat S* 53, 7 (2001): p. 29-+.
31. T. Suter, R.C. Alkire, *J Electrochem Soc* 148, 1 (2001): p. B36-B42.
32. A.W. Hassel, K. Fushimi, M. Seo, *Electrochem Commun* 1, 5 (1999): p. 180-183.
33. A. Bauereiss, T. Scharowsky, C. Korner, *J Mater Process Tech* 214, 11 (2014): p. 2522-2528.
34. A.J. Sedriks, Electrochemical Society., *Corrosion of Stainless Steels*, 2nd ed.(New York: Wiley, 1996).
35. G.H. Eichelman, F.C. Hull, *T Am Soc Metal* 45, (1953): p. 77-104.
36. S. Kou, *Welding Metallurgy*, 2nd ed.(Hoboken, N.J.: Wiley-Interscience, 2003).
37. A.K. Sinha, *Physical Metallurgy Handbook*, (New York: McGraw-Hill, 2003).
38. X.P. Ma, L.J. Wang, S.V. Subramanian, C.M. Liu, *Metall Mater Trans A* 43a, 12 (2012): p. 4475-4486.
39. M.A. Streicher, *J Electrochem Soc* 103, 7 (1956): p. 375-390.
40. A.A. Hermas, K. Ogura, S. Takagi, T. Adachi, *Corrosion* 51, 1 (1995): p. 3-10.
41. M.A. Baker, J.E. Castle, *Corrosion Science* 33, 8 (1992): p. 1295-1312.
42. T. Raghu, S.N. Malhotra, P. Ramakrishnan, *Corrosion* 45, 9 (1989): p. 698-704.
43. A.V.C. Sobral, W. Ristow, D.S. Azambuja, I. Costa, C.V. Franco, *Corrosion Science* 43, 6 (2001): p. 1019-1030.
44. I. Costa, S.O. Rogero, O.V. Correa, C.T. Kunioshi, M. Saiki, *Advanced Powder Technology Iv* 498-499, (2005): p. 86-92.
45. ASM International. Handbook Committee., *Asm Handbook*, 10th editon. ed.(Materials Park, Ohio: ASM International, 1990).
46. G.S. Frankel, "Localized Corrosion Phenomenology and Controlling Parameters," 2002.
47. I. Costa, C.V. Franco, C.T. Kunioshi, J.L. Rossi, *Corrosion* 62, 4 (2006): p. 357-365.
48. T. Mathiesen, E. Maahn, *Powder Metallurgy Worl Congree*, (1994): p. 2089-2092.
49. J.W. Oldfield, W.H. Sutton, *British Corrosion Journal* 13, 1 (1978): p. 13-22.
50. M.I. Abdulsalam, H.W. Pickering, *J Electrochem Soc* 145, 7 (1998): p. 2276-2284.
51. Y. Xu, H.W. Pickering, *J Electrochem Soc* 140, 3 (1993): p. 658-668.
52. A. Turnbull, J.G.N. Thomas, *J Electrochem Soc* 129, 7 (1982): p. 1412-1422.
53. L.A. DeJong, R.G. Kelly, *Elec Soc S* 98, 17 (1999): p. 678-688.
54. C. Molins, J.A. Bas, J. Planas, *Advances in Powder Metallurgy & Particulate Materials - 1992, Vol 5*, (1992): p. 345-357.
55. M.H. Tikkanen, *Scand J Metall* 11, 5 (1982): p. 211-215.
56. A.U. Malik, N.A. Siddiqi, I.N. Andijani, *Desalination* 97, 1-3 (1994): p. 189-197.
57. D. Nakhaie, M.H. Moayed, *Corros Sci* 80, (2014): p. 290-298.
58. M. Esfandiari, H. Dong, *Surf Coat Tech* 202, 3 (2007): p. 466-478.

FIGURE CAPTIONS

Table 1. 17-4 PH Steel Composition (wt%) values for Wrought and LPBF samples determined by independent testing laboratory NSL Analytical using LECO Furnace, ICP-MS, and ICP.

Table 2. Average E_{corr} and i_{corr} of Wrought vs. LPBF 17-4 PH exposed to 0.6 M NaCl solution compared to literature values for wrought 17-4 PH.[56-58]

Table 3. Average of E_{corr} and i_{corr} values of Pores vs. Non-porous surfaces of LPBF 17-4 PH exposed to 0.6 M NaCl solution in a micro-electrochemical cell.

Figure 1. Schematic of LPBF 17-4 PH build direction and surfaces tested.

Figure 2. Histogram plot displaying distribution of maximum pore diameters measured on the LPBF 17-4 PH top surface and cross sectional surface.

Figure 3. SEM secondary electron (SE) micrographs of LPBF 17-4 PH a) perpendicular to build direction (top surface) and b) in plane with the build direction (cross-section).

Figure 4. SEM and EDS maps of LPBF 17-4 PH, unexposed. A) SE micrograph with EDS Spectra locations, b) Cr EDS map, and c) comparison of spectra taken at an undissolved particle, the pore surface, and the polished surface.

Figure 5. Back scattered SEM micrographs of a a) LPBF pore and d) LPBF non-porous surface of 17-4 PH and corresponding WDS maps for b) and e) Cr and c) and f) O.

Figure 6. Optical images of 17-4 PH etched using Viella's reagent which is comprised of a solution of 100 mL ethanol, 1 g picric acid, and 5 mL concentrated hydrochloric acid. A) Wrought and b) LPBF 17-4 PH.

Figure 7. 24 h open circuit potential of wrought and LPBF 17-4 PH in quiescent 0.6 M NaCl.

Figure 8. Anodic polarization measurements on wrought and LPBF 17-4 PH after a) 1 h and b) 24 h open circuit immersion in quiescent 0.6 M NaCl.

Figure 9. Cathodic polarization measurements on wrought and LPBF 17-4 PH after a 1 h open circuit immersion in quiescent 0.6 M NaCl.

Figure 10. Micro-electrochemical cell experiments on a large pore ($d \geq 50$ µm) vs. a minimally porous area (pores of $d \leq 10$ µm) of the LPBF 17-4 PH sample exposed to quiescent 0.6 M NaCl for a) 1 h E_{OCP} and b) an anodic scan from -200 mV vs. E_{OCP} to +700 mV vs. E_{OCP} at a scan rate of 1 mV/s. Optical images c) and d) exemplify minimally porous areas and areas with large pores respectively examined by micro-electrochemical cell.

Figure 11. Micro-electrochemical cell experiments on a large pore (d ≥ 50 µm) vs. a minimally porous area (pores of d ≤ 10 µm) of the LPBF 17-4 PH sample exposed to quiescent 0.6 M NaCl for a) 24 h E_{OCP} and b) an anodic scan from -200 mV vs. E_{OCP} to +700 mV vs. E_{OCP} at a scan rate of 1 mV/s.

Figure 12. SEM SE micrographs of LPBF 17-4 PH after a 7 day open circuit exposure in quiescent 0.6 M NaCl. A) SEM micrograph illustrating area where corrosion product build up has flaked off revealing pore beneath and b) corrosion product build up over a pore.

Table 1. 17-4 PH Steel Composition (wt%) values for Wrought and LPBF samples determined by independent testing laboratory NSL Analytical using LECO Furnace, ICP-MS, and ICP.

Sample	C	Cb	Cr	Cu	Fe	Mn	Mo	N	Ni	O	P	S	Si	Ta
Wrought	0.047	0.23	15.19	3.21	75.6	0.53	0.23	0.023	4.54	0.014	0.022	<0.001	0.17	<0.001
LPBF	0.017	0.29	16.02	3.95	74.9	0.22	0.025	0.036	4.12	0.068	0.013	0.002	0.33	<0.001

Table 2. Average E_{corr} and i_{corr} of Wrought vs. LPBF 17-4 PH exposed to 0.6 M NaCl solution compared to literature values for wrought 17-4 PH.[56-58]

Sample	1 h E_{OCP}		24 h E_{OCP}	
17-4 PH	**E_{corr} (V_{SHE})**	**i_{corr} (A/cm^2)**	**E_{corr} (V_{SHE})**	**i_{corr} (A/cm^2)**
Wrought	0.049 +/- 0.023	2.30×10^{-8} +/- 3×10^{-9}	0.265 +/- 0.094	2.73×10^{-9} +/- 4×10^{-11}
LPBF	-0.052 +/- 0.055	2.41×10^{-7} +/- 2×10^{-7}	-0.017 +/- 0.061	7.28×10^{-8} +/- 2×10^{-8}
Literature Values	-	-	0.016* +/- 0.004	-

*Taken from exposures of 15 min to 40 h.

Table 3. Average of E_{corr} and i_{corr} values of Pores vs. Non-porous surfaces of LPBF 17-4 PH exposed to 0.6 M NaCl solution in a micro-electrochemical cell.

LPBF 17-4 PH	E_{corr} (V_{SHE})	i_{corr} (A/cm^2)
Non-porous Surface	0.115 +/- 0.02	1.71×10^{-7} +/- 1×10^{-7}
Pores	0.092 +/- 0.016	2.17×10^{-7} +/- 2×10^{-7}
Wrought	0.182 +/- 0.012	2.12×10^{-7} +/- 9×10^{-8}

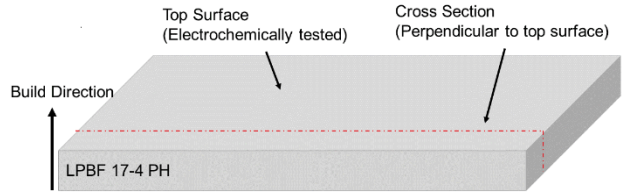

Figure 1. Schematic of LPBF 17-4 PH build direction and surfaces tested.

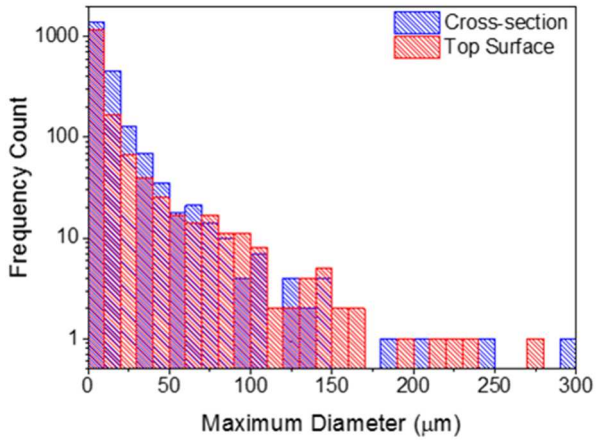

Figure 2. Histogram plot displaying distribution of maximum pore diameters measured on the LPBF 17-4 PH top surface and cross sectional surface.

a) b)

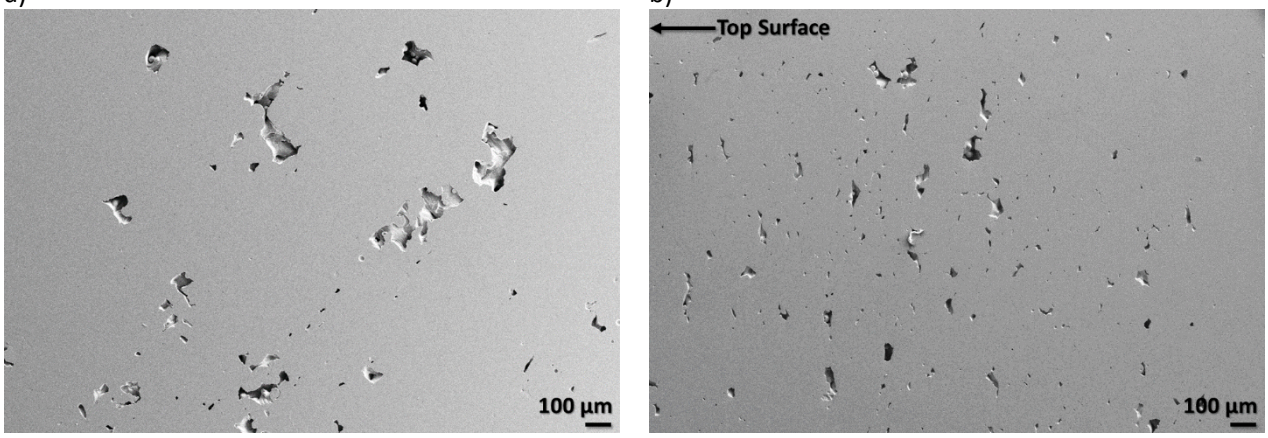

Figure 3. SEM secondary electron (SE) micrographs of LPBF 17-4 PH a) perpendicular to build direction (top surface) and b) in plane with the build direction (cross-section).

a) b)

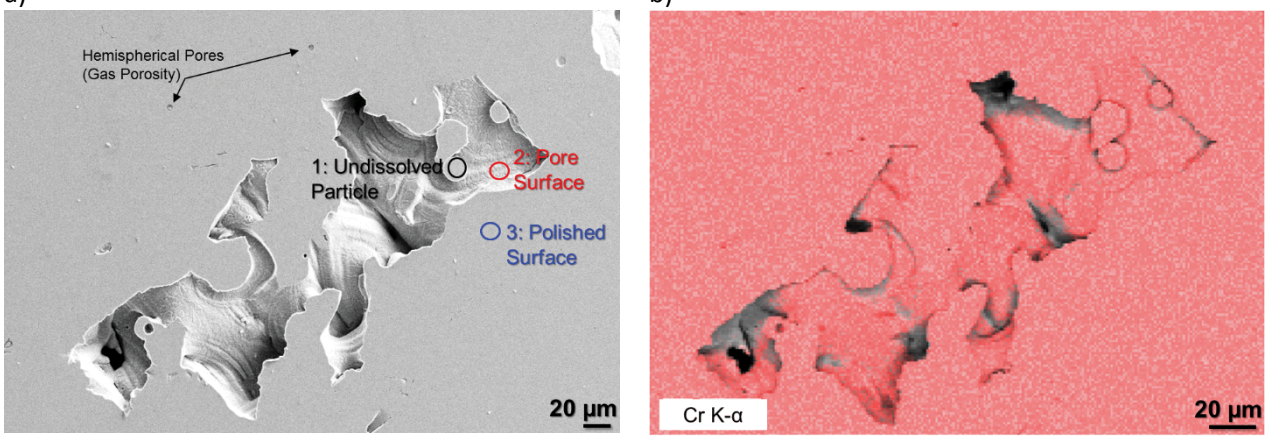

c)

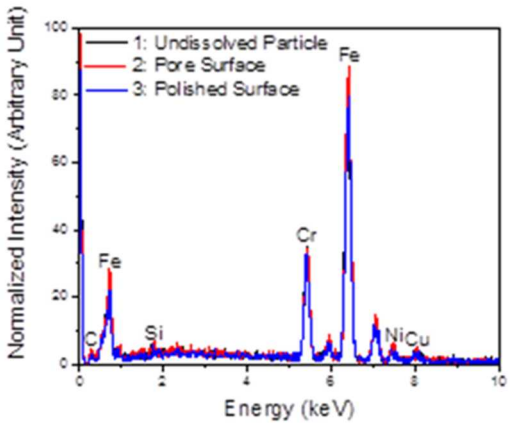

Figure 4. SEM and EDS maps of LPBF 17-4 PH, unexposed. A) SE micrograph with EDS Spectra locations, b) Cr EDS map, and c) comparison of spectra taken at an undissolved particle, the pore surface, and the polished surface.

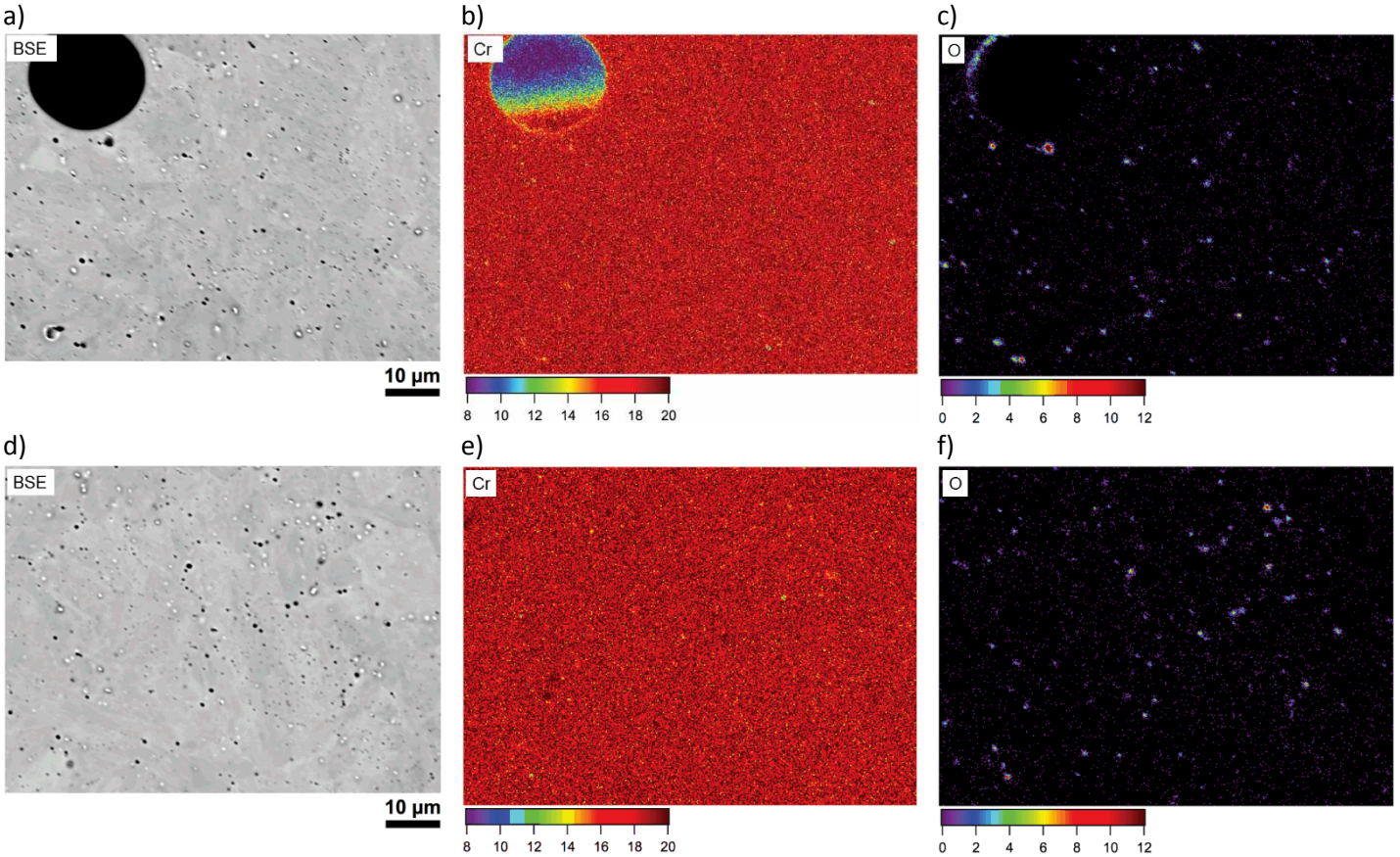

Figure 5. Back scattered SEM micrographs of a a) LPBF pore and d) LPBF non-porous surface of 17-4 PH and corresponding WDS maps for b) and e) Cr and c) and f) O.

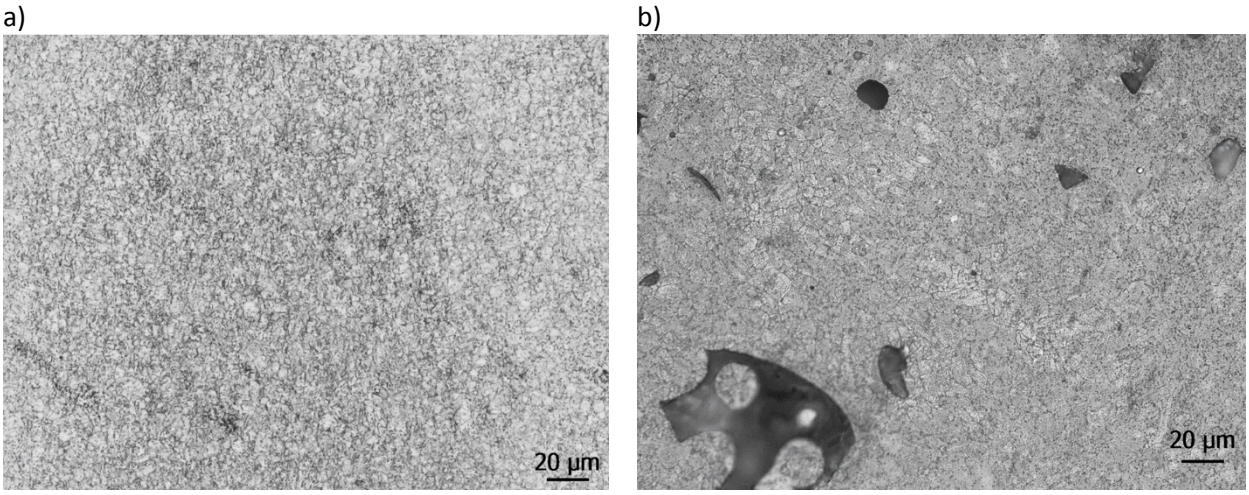

Figure 6. Optical images of 17-4 PH etched using Viella's reagent which is comprised of a solution of 100 mL ethanol, 1 g picric acid, and 5 mL concentrated hydrochloric acid. A) Wrought and b) LPBF 17-4 PH.

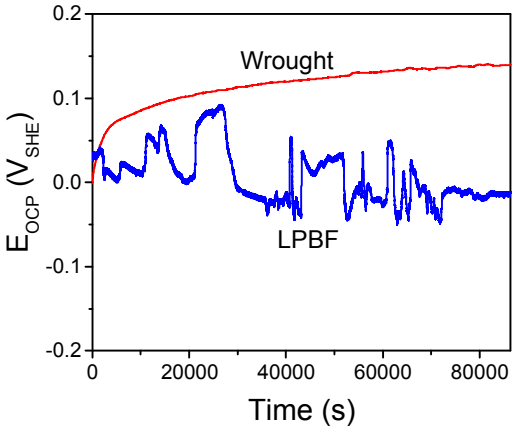

Figure 7. 24 h open circuit potential of wrought and LPBF 17-4 PH in quiescent 0.6 M NaCl.

a)

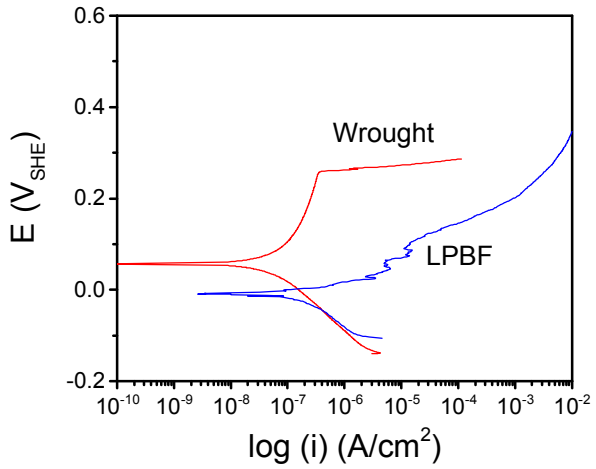

b)

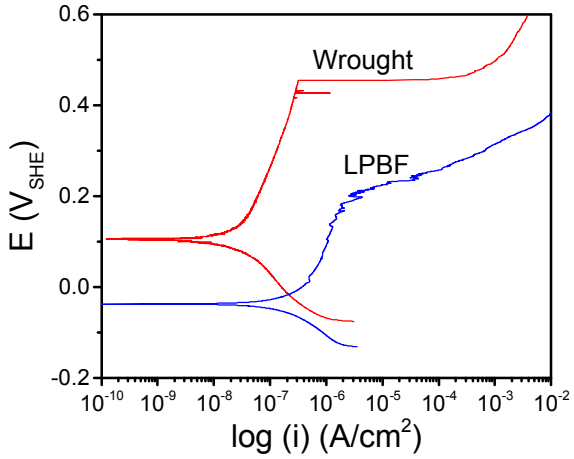

Figure 8. Anodic polarization measurements on wrought and LPBF 17-4 PH after a) 1 h and b) 24 h open circuit immersion in quiescent 0.6 M NaCl.

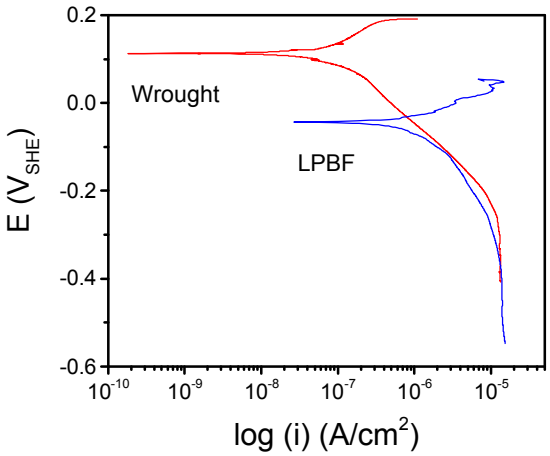

Figure 9. Cathodic polarization measurements on wrought and LPBF 17-4 PH after a 1 h open circuit immersion in quiescent 0.6 M NaCl.

a)

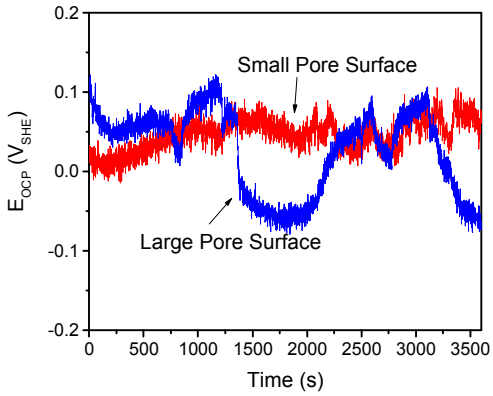

b)

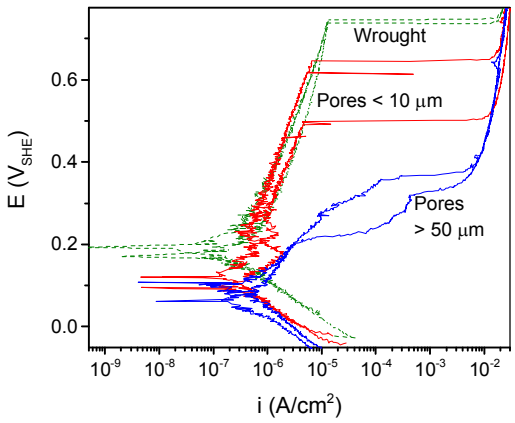

c)

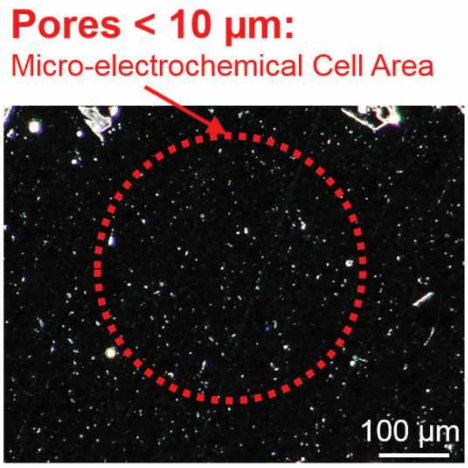

d)

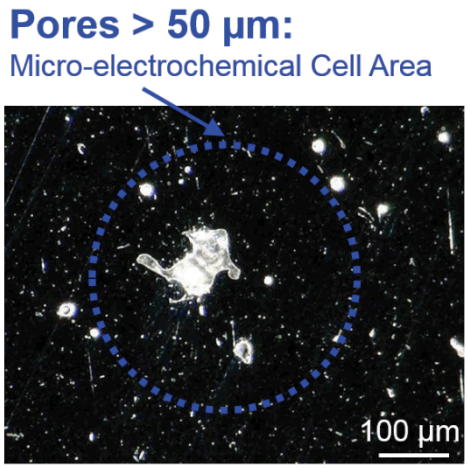

Figure 10. Micro-electrochemical cell experiments on a large pore (d ≥ 50 µm) vs. a minimally porous area (pores of d ≤ 10 µm) of the LPBF 17-4 PH sample exposed to quiescent 0.6 M NaCl for a) 1 h E_{OCP} and b) an anodic scan from -200 mV vs. E_{OCP} to +700 mV vs. E_{OCP} at a scan rate of 1 mV/s. Optical images c) and d) exemplify minimally porous areas and areas with large pores respectively examined by micro-electrochemical cell.

a) b)

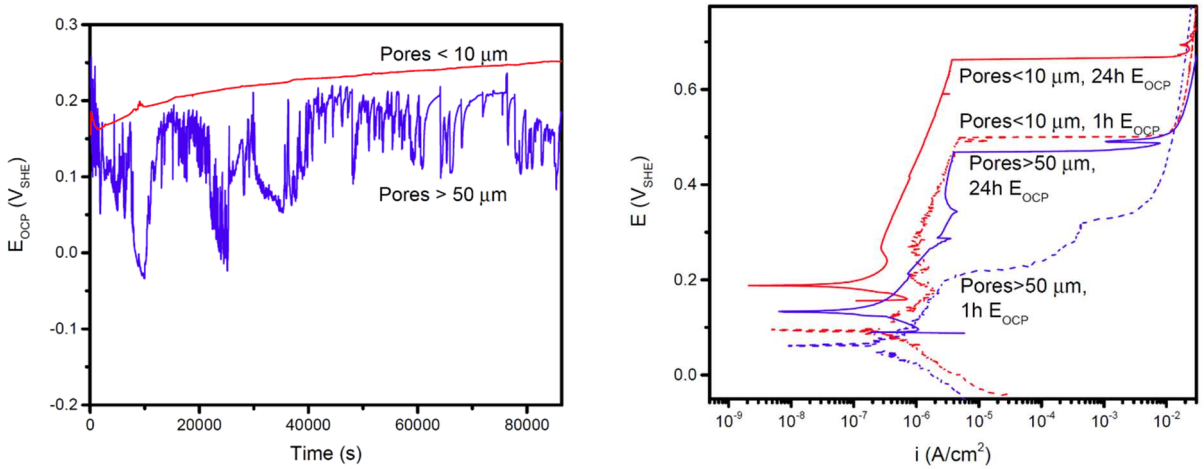

Figure 11. Micro-electrochemical cell experiments on a large pore (d ≥ 50 µm) vs. a minimally porous area (pores of d ≤ 10 µm) of the LPBF 17-4 PH sample exposed to quiescent 0.6 M NaCl for a) 24 h E_{OCP} and b) an anodic scan from -200 mV vs. E_{OCP} to +700 mV vs. E_{OCP} at a scan rate of 1 mV/s.

a) b)

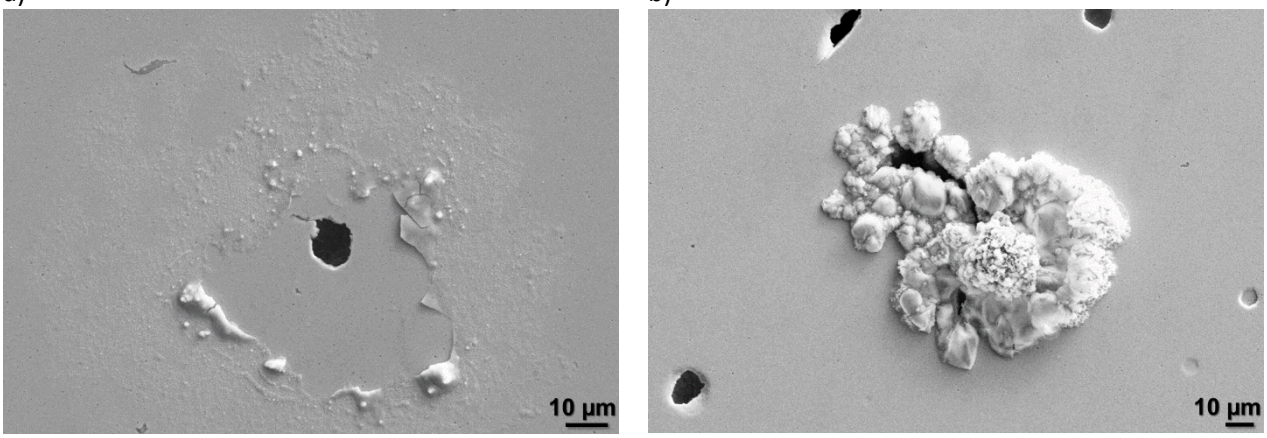

Figure 12. SEM SE micrographs of LPBF 17-4 PH after a 7 day open circuit exposure in quiescent 0.6 M NaCl. A) SEM micrograph illustrating area where corrosion product build up has flaked off revealing pore beneath and b) corrosion product build up over a pore.